Electron beam lithography on curved or tilted surfaces

Simulations and experiments

Arat, Kerim T.; Zonnevylle, Aernout C.; Ketelaars, Wilhelmus S.M.M.; Belic, Nikola; Hofmann, Ulrich; Hagen, Cornelis W.

Important note
To cite this publication, please use the final published version (if applicable).
Please check the document version above.

Electron beam lithography on curved or tilted surfaces: Simulations and experiments

Kerim T. Arat (iD), Aernout C. Zonnevylle, Wilhelmus S. M. M. Ketelaars, Nikola Belic, Ulrich Hofmann, and Cornelis W. Hagen

View Online   Export Citation   CrossMark

ARTICLES YOU MAY BE INTERESTED IN

Electron beam lithography on curved or tilted surfaces: Simulations and experiments

Kerim T. Arat,[1,a)] Aernout C. Zonnevylle,[2] Wilhelmus S. M. M. Ketelaars,[2] Nikola Belic,[3] Ulrich Hofmann,[3] and Cornelis W. Hagen[1]

[1]*Faculty of Applied Sciences, Delft University of Technology, Lorentzweg 1, 2628CJ Delft, The Netherlands*
[2]*Raith B.V., De Dintel 27a, 5684PS Best, The Netherlands*
[3]*GenISys GmbH, Eschenstrasse 66, 82024 Taufkirchen, Germany*

There is a growing interest for patterning on curved or tilted surfaces using electron beam lithography. Computational proximity correction techniques are well established for flat surfaces and perpendicular exposure, but for curved and tilted surfaces adjustments are needed as the dose distribution is no longer cylindrically symmetric with respect to the surface normal. A graphical processing unit - accelerated 3D Monte Carlo simulation, based on first-principle scattering models, is used to simulate the asymmetric dose distribution. Based on that, an approximate adjustment is made to an existing high-performance proximity effect correction (PEC) algorithm aimed at the correct exposure of a pattern of nanowires on a 17° tilted surface. It was experimentally verified that using the adjusted PEC indeed leads to a more uniform exposure on tilted surfaces. *Published by the AVS.*
https://doi.org/10.1116/1.5120632

I. INTRODUCTION

In electron beam lithography (EBL), patterns are written in an electron sensitive material (resist) using a focused electron beam. During the exposure, the interaction of the electrons and the resist-substrate stack changes the resist's solubility. Depending on the tone of the resist, usually consisting of polymers, the change in the solubility occurs by breaking bonds in the polymer network or creating a stronger network by cross-linking the monomers to neighboring monomers. For instance, in a positive resist, when enough bonds are broken in a certain area, this area becomes soluble to a developer and the patterned feature shows up as a recessed shape in the resist. To control the size of the pattern, it requires control over the distribution of broken bonds, which is related to the electron dose distribution. As the electrons scatter in the resist-substrate stack they spread laterally, influencing the exposure of neighboring areas. This so-called proximity effect can be corrected if this lateral spread, often indicated as the point spread function (PSF), is known. The correction of this effect by adjusting the number of incident beam electrons (dose) is known as proximity effect correction (PEC), which has become standard in EBL.[1–3] When the electron beam is incident perpendicularly to a flat surface [Fig. 1(a)], the PSF is cylindrically symmetric around the surface normal, a property that is often used for PSF calculations.[4–10] Once the PSF is known, the electron dose can be calculated for patterns in a given layout.

Recently, there is a growing interest to pattern tilted surfaces by EBL.[11–15] In this case, the beam has a non-zero angle with the surface normal [Fig. 1(b)]. For such applications, where the cylindrical symmetry no longer exists, the standardly used PSF calculation techniques are no longer suitable, and the PEC techniques[1,2,16] need to be adjusted accordingly.

In this study, first the PSFs are simulated for a perpendicular surface and tilted surface using a 3D Monte Carlo simulator[17] and the asymmetry in the tilted case is verified experimentally. Then, an approximate method is used to adapt an existing high-performance PEC algorithm to the asymmetric PSF, and the resulting exposure of a tilted resist-substrate stack is compared to an exposure using the regular PEC, based on the symmetric PSF. In the discussion, the pitfalls of using the regular PEC based on the cylindrically symmetric PSF, when exposing tilted surfaces, will be addressed.

II. MONTE CARLO SIMULATOR

A common way to determine the PSF is using Monte Carlo simulations. It is crucial to use reliable electron-matter interaction models in the simulator, especially for low energy electron scattering since the bond-breaking rate is highest at low energies.[18] We have used the *e-scatter* Monte Carlo simulator,[17] which contains first-principle elastic and inelastic scattering models and runs on a graphical processing unit to benefit from parallel processing.

In *e-scatter*, the elastic scattering cross sections are based on the relativistic Mott cross sections including solid-state effects using a "muffin-tin" approximation for the potential. These cross sections are calculated by ELSEPA (Ref. 19) and used for energies above 200 eV. At very low energies, the electrons dominantly interact with the lattice rather than the atomic potential. Therefore, the interaction of electrons with acoustic phonons is taken into account[17,20] at energies below 100 eV, where the Mott description is no longer applicable.[21] For energies between 100 and 200 eV, an interpolation between the cross sections for the two processes is used.[17] The inelastic scattering is modeled by using the dielectric function.[21] In addition, an electron trapping model[22] is

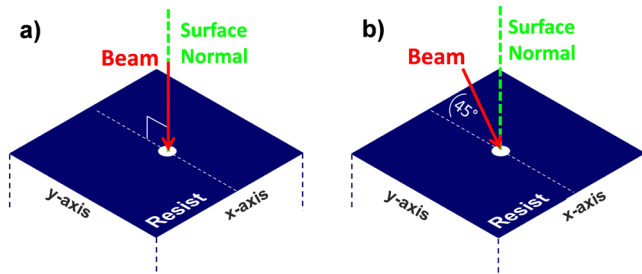a)Electronic mail: k.t.arat@tudelft.nl

FIG. 1. Exposure at different angles: the incident beam (arrow) (a) is perpendicular to the resist surface and (b) has a 45° angle with the surface normal (dashed line).

used for the resist. The details of the models are explained in chapter 3 of the thesis of Verduin.[17] Figure 2 shows the elastic and inelastic mean free paths of the materials used in this study, i.e., a silicon (Si) substrate and polymethyl methacrylate (PMMA) as resist.

As the simulator models individual inelastic events, it would, in principle, allow for the determination of the number of bond-breaking events if the probability for bond-breaking was known. However, the cross sections for bond breaking are not well known. From the literature,[18] it is known that the status of the carbon-carbon backbone of the resist molecule plays an important role in the determination of its solubility. Wu and Neureuther[23] reported that the bond-breaking cross section vanishes at energies below 4.9 eV. In other words, electrons with energy lower than 4.9 eV cannot break a bond. Although the zero of energy is not defined by the authors,[23] it is assumed here that it is the bottom of the valence band. Due to the lack of known bond-breaking cross sections, a common approach is to store the energy lost in an inelastic event or a trapping event, in the volume element (voxel) of resist where the event occurred,[7,8,24] provided that more energy than a threshold value, assumed here as 4.9 eV, is lost. The number of broken bonds is then assumed to be
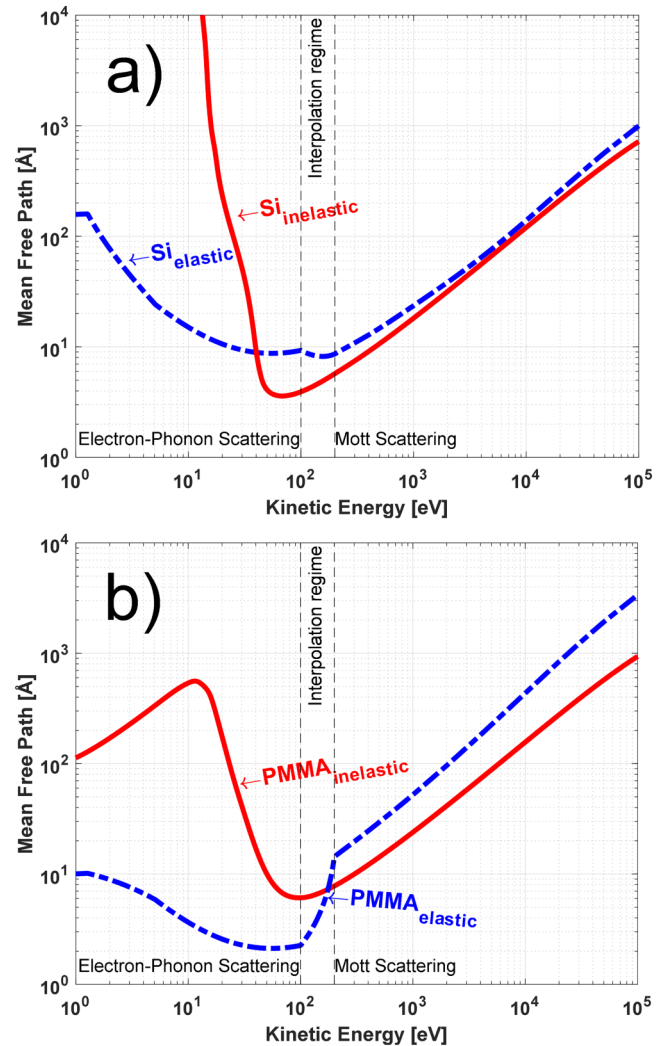
FIG. 2. Elastic (dashed lines) and inelastic (solid lines) mean free paths of the materials used in this study; (a) silicon and (b) PMMA. The vertical dashed lines serve to distinguish the electron-phonon scattering regime (low energies) and the Mott scattering regime (high energies).
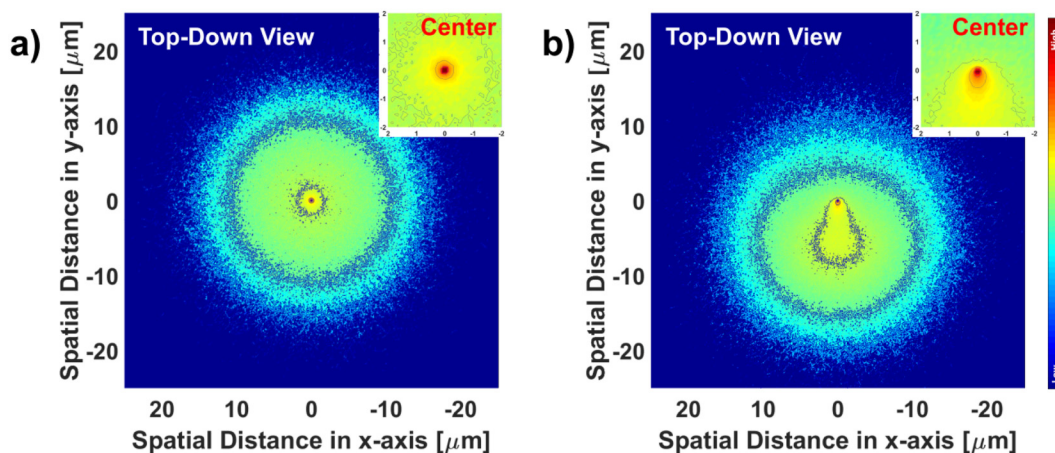
FIG. 3. Top-down representation of simulated energy deposition profiles (PSF). The incident beam is (a) perpendicular to the resist surface and (b) under an angle of 45° with the surface normal. The insets (in micrometer) magnify the center of the exposure. The color map (logarithmic scale in energy/volume) qualitatively represents the energy deposition.
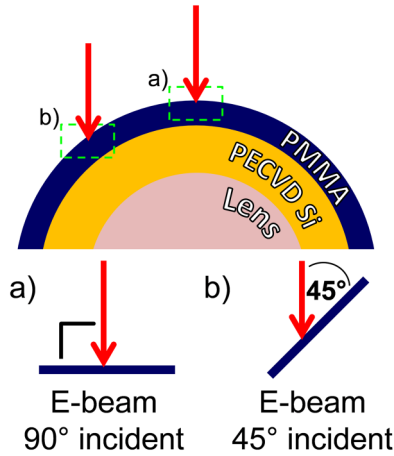
FIG. 4. Exposure of a curved surface: the sample stack consists of 4 μm of PECVD a-Si on top of a spherical glass lens (radius = 25.7 mm) and an ~100 nm layer of PMMA spin-coated on top. (a) Location of perpendicular exposure and (b) location of exposure under 45° tilt with the surface normal.

proportional to the deposited energy per voxel, and the distribution of energy deposited in the resist is associated with the PSF.

III. POINT EXPOSURE OF RESIST ON A CURVED SURFACE

The Monte Carlo simulator is used to calculate the PSF for the electron exposure of an Si-substrate/100 nm PMMA stack in two cases: (i) exposure perpendicular to the stack and (ii) exposure under 45° with the surface normal of the stack. The beam energy is 50 keV, and a zero-diameter beam is assumed. The voxels in which the deposited energy is stored have a lateral size of 25×25 nm^2 and 100 nm perpendicular to the substrate (equal to the resist thickness). Figure 3 shows the top-down views, i.e., viewing along the surface normal, of the PSFs in the resist, obtained in the two cases. In Fig. 3(a), the PSF for perpendicular exposure is observed to be nicely cylindrically symmetric, both near the very center (inset) and further from the point of incidence. In contrast, the PSF for tilted exposure, as shown in Fig. 3(b), is asymmetric and shifted compared to the perpendicular exposure case.

To experimentally verify the simulation results, a spherical glass lens was coated with a 4 μm thick layer of PECVD (plasma enhanced chemical vapor deposition) a-Si, and spin coated with an ~100 nm thick layer of 495 k PMMA in 3% Anisole. It was soft-baked for 10 min at 180 °C.

The exposure was done at an electron beam energy of 50 keV, a beam current of 10 nA, and the exposure time was 2 s. The sample was exposed at two different locations. The sample geometry is depicted in Fig. 4. The first location was exposed along the surface normal, and the second at a 45° tilt with respect to the surface normal.

After development in methyl isobutyl ketone (MIBK) in 60 s, rinsed for 60 s with isopropanol (IPA) and dried with dry nitrogen gas. The exposed locations were imaged along the surface normal using an optical microscope. A similar approach to visualize the interaction volume is described by Rishton and Kern.[10]

The results, shown in Fig. 5, qualitatively agree with the profiles obtained from the simulation. The asymmetric profile obtained for exposure of tilted substrates is so distinctly different from the symmetric one for perpendicular exposure that standard PEC techniques, based on cylindrically symmetric PSFs, are not suitable for exposures of tilted or curved samples.

IV. PROXIMITY EFFECT CORRECTED PATTERNING OF TILTED SURFACES

In contrast to other applications[24] where 3D PEC is required, we here address how to optimize the exposure of a pattern on a tilted substrate. First, a test pattern was designed, suitable to clearly show the difference when an asymmetric PSF in the proximity effect correction is used instead of the usual symmetrical one. The pattern is written at 50 keV beam energy on a 17° tilted Si substrate with a 150 nm thick layer of PMMA resist, as shown schematically in Fig. 6. On this substrate, the same pattern was written twice with two different PSFs used for the PEC. The PEC of the first exposure was done with the symmetrical PSF for perpendicular exposure, and the PEC of the second exposure was done by taking into account the asymmetrical PSF for tilted exposure.

The test pattern consists of a large square (50×50 μm^2) embraced at the upper right side and the lower left side by lines and spaces, as shown in Fig. 7. The lines are equal in width at both sides. The nominal linewidth is 0.1 μm, and the pitch is 0.3 μm. The size of the square was chosen such that a significant amount of background dose contributes to the exposure of the pattern of lines and spaces. It is noted that PMMA is a positive resist, and the exposed lines in the pattern will appear as trenches on the sample after development.

On a flat substrate, the proximity effect of exposing the middle square would be the same for both left- and
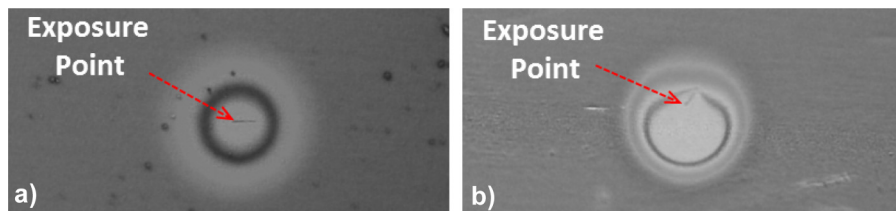

FIG. 5. Optical microscopy images of point exposures of a 100 nm thick PMMA layer on a glass sphere, coated with a-Si, after development. (a) The exposure is perpendicular to the substrate. (b) The exposure is at a 45° (±2°) tilt from the surface normal. The electron beam energy was 50 keV, the beam current was 10 nA, and the exposure time was 2 s. Horizontal field view is ~120 μm.
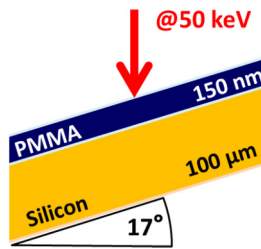
FIG. 6. Cross-sectional view of exposure on a 17° tilted substrate. Note that structures on the right-hand side are positioned higher along the vertical coordinate than structures on the left-hand side.

FIG. 7. Test pattern consisting of a $50 \times 50 \, \mu m^2$ square, embraced by two patterns of lines ($0.1 \, \mu m$ wide) and spaces ($0.2 \, \mu m$ wide) on the left- and right-hand sides of the square. (a) Overview and (b) zoomed-in drawing of the left-hand side of the pattern. The right-hand side (not shown as a zoomed-in drawing) is the mirror image of the left-hand side.

right-hand patterns of lines and spaces, using the symmetrical PSF in the PEC. However, in the tilted substrate case, the effect of the middle square exposure will contribute more to the exposure of the lines on the left than to the exposure of the lines on the right of the square due to the asymmetrical PSF. This will cause the lines on the left to develop differently from the lines on the right unless the exposure dose is corrected using the proper PSF, i.e., the asymmetrical PSF for exposure of tilted surfaces.

The PSFs needed for the PEC are obtained using Monte Carlo simulation. Figure 8 shows the two simulation geometries: perpendicular beam exposure [Fig. 8(a)] and 17° tilted beam exposure [Fig. 8(b)].

The simulation volume is discretized in cylindrical coordinates for computational efficiency. The radial axis is divided into 76 points, logarithmically increasing from 1 nm to $50 \, \mu m$. The azimuthal plane is divided into 60 segments of 6° each. The resist is discretized in 10 layers along the surface normal, each 15 nm thick, to enable an analysis of the asymmetry in 3D. In the simulation, a zero-diameter beam is used with 10^7 electrons.

The simulated PSFs in the topmost 15 nm thick layer, for both the perpendicular and tilted beam geometry, are shown in Fig. 9. The deposited energy density is plotted vs the x-coordinate, that is, the direction perpendicular to both the perpendicular and the tilted beam. As expected, the PSF is symmetric for the perpendicular beam (0°) and asymmetric for the tilted (17°) beam. In the latter case, more energy is deposited at the left-hand side (lhs), and the entire profile is shifted to the left (note the log-scale). The discontinuity at
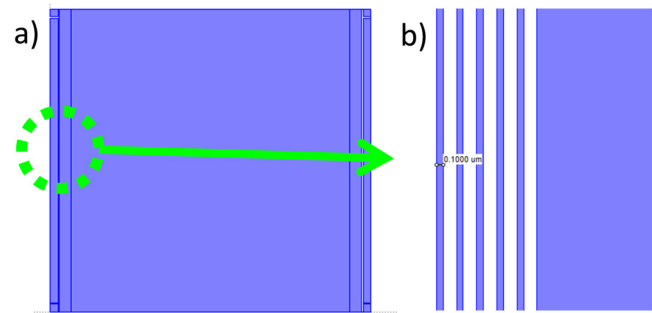
the center of the PSFs is due to the discretization and the logarithmic scale. When the tilted zero-diameter beam enters the resist, it travels mostly through the left-hand voxels with a height of 15 nm.

In Fig. 10, both PSFs are shown, along the x-axis, in the bottom layer of the resist, in contact with the substrate. As in the upper layers, the deposited energy profile is shifted to the left for the tilted beam. Also, a peak in the PSF is visible, which migrates to the left when the beam intersects deeper layers, amounting to a shift of 40 nm at a depth of 150 nm. This peak already appears in the first layer, seen as a plateau in Fig. 9 due to the logarithmic scale.

The logarithmic plots of Figs. 9 and 10 are convenient to visualize the short-range effects, i.e., close to the point of incidence, but the long-range effect is less well visible. The latter is better visualized when plotted on a linear scale, such as in Fig. 11. Here, it is seen clearly that the tilted exposure profile is shifted to the left by ~$2.1 \, \mu m$.

In Fig. 12, the PSFs are plotted along the y-axis (x = 0) for both perpendicular and tilted substrates. There is no asymmetry observed in this case because there is no beam tilt with respect to this axis. However, the peak in the deposited energy drops dramatically in the bottom layer of the resist for the tilted beam, see Fig. 12(b). This is because the beam intersection with that layer has shifted from the point of incidence (x,y) = (0,0).
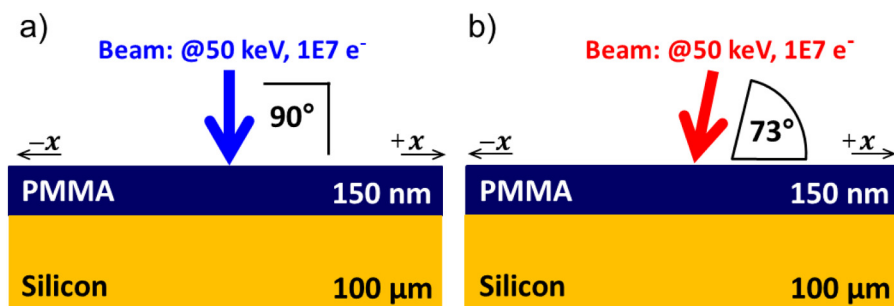
FIG. 8. Simulation geometries to obtain the PSFs: 50 keV exposure of 150 nm PMMA resist on top of a $100 \, \mu m$ thick silicon substrate with the beam (a) perpendicular to the substrate and (b) at 17° tilted from the surface normal. A zero-diameter beam is used containing 107 electrons. The color code of the beams, blue solid line represents the perpendicular beam and red dashed line the tilted beam, is maintained in the following figures in the color online version.

FIG. 9. PSF comparison for the perpendicular and the tilted beam in the top-most surface layer (15 nm thick), plotted along the x-axis (the in-plane horizontal direction in the inset). The symmetrical solid blue curve is obtained for the perpendicular beam; the dashed red curve is obtained for the 17° tilted beam.

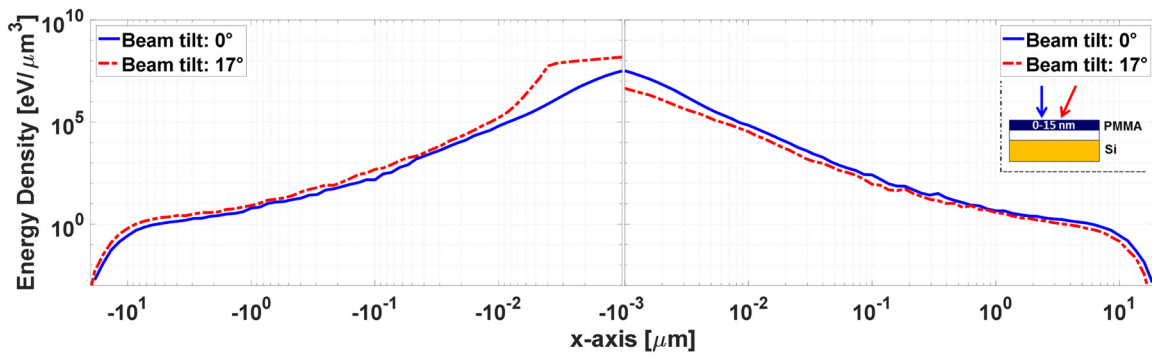To summarize the results of the PSF simulations, the long-range shift of the PSF due to tilted exposure is in the order of micrometers which should be corrected for with PEC to minimize its influence on the exposure of neighboring features. The short-range effects, which are the beam shift (at maximum ~40 nm here), beam diameter, and beam straggling, are smaller than the feature size (100 nm). Therefore, we do not expect that the short-range effects will significantly influence the linewidth, but the line shape may be affected. We will address this later.

Now we turn to the question of how to adapt the PEC for the tilted exposure PSF. The best result would be obtained by using the full 3D PSF in the PEC algorithm, but that would be computationally very time consuming, and we consider the design of an entirely new algorithm beyond the context of this work. Instead, we chose to use the PEC function of a commercially available e-beam software package [BEAMER (Ref. 25)] for the proximity correction in 2D and modify the symmetric PSF. We start with separating the untilted exposure PSF, in the resist layer between 75 and 90 nm depth, into two functions: a short-range function f_{sr} that best matches the PSF up to ~20 nm and a long range function f_{lr} that best matches the PSF above ~1 μm. Both functions are rotationally symmetric around the beam axis and they are shown in Fig. 13. For the exposure of tilted surfaces we found that the long-range shift of the energy distribution, originating from the backscattered electrons, is much larger than the shift of the short-range distribution. For simplicity, we will ignore the latter shift, i.e., the same f_{sr} is

used for tilted and untilted exposures. The effect of the tilted exposure is solely approximated by shifting the function f_{lr} over 2.1 μm. Note that we are shifting the entire rotationally symmetric distribution f_{lr} in one direction over 2.1 μm, ignoring the fact that the real distribution is not rotationally symmetric at all. Exposing the test pattern of Fig. 7 and adding up the dose received by the resist, using the approximated long-range PSF, f_{lr} in Fig. 13, one arrives at the long-range dose distributions of the tilted and nontilted exposures shown in Fig. 14.

To find the total dose distribution, the long-range and short-range effects are summed (see Fig. 15) where the long-range distribution is the shifted distribution for the 17° tilted beam exposure and the short-range distribution is assumed to be the one for the nontilted beam exposure.

Once the dose calculation is done, the PEC algorithm optimizes the exposure doses iteratively by calculating the normalized local exposure by convolving the PSF with the corresponding 2D coverage matrix of the layout. For the final dose assignment, the original pattern is divided into fragments required to assure optimal transcription into the exposure format. In Fig. 16, the dose-corrected exposure layouts, with and without accounting for the tilt, are shown. The color map shows the variation of dose (red—high, blue—low regions in the color online version) over the pattern. The image of the tilt-corrected Fig. 16(b) shows the exposure asymmetry required to compensate for the asymmetric PSF. The lines on the right require more dose than the lines on the left due to the left shift of the long-range distribution. In Fig. 16(c), the
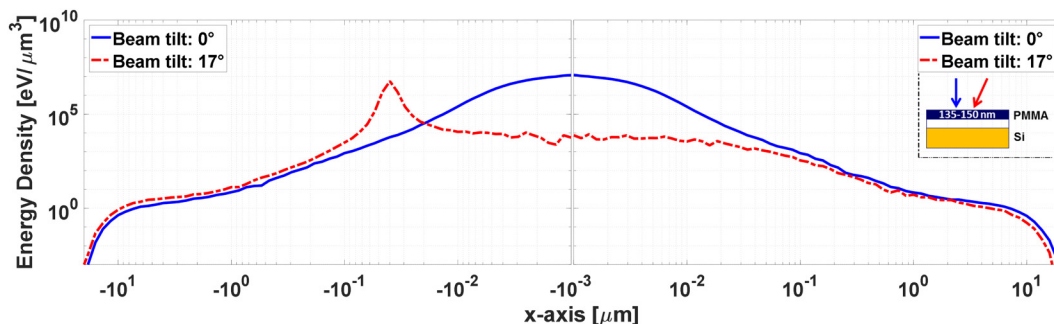

FIG. 10. PSF comparison for the perpendicular and tilted beam in the bottom layer (15 nm thick).
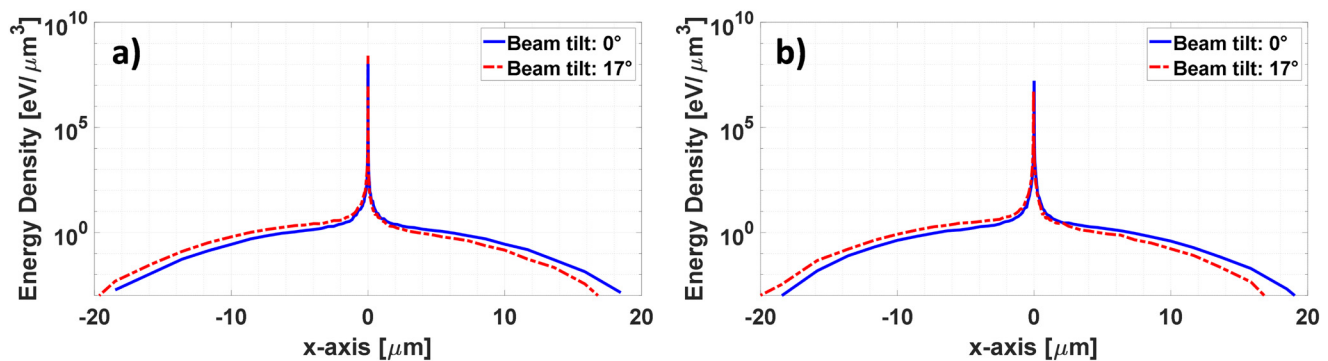
FIG. 11. Comparison of the PSFs on a linear scale to show the asymmetry along the x-axis, i.e., the long-range shift: (a) in the top-most layer (vacuum interface) and (b) in the bottom layer (substrate interface).

PEC distributes equal amounts of dose to both the left- and right-hand side (rhs) lines without considering the tilt of the sample, as the PSF is symmetric.

V. EXPERIMENTS

The exposure was performed with a Raith EPBG 5200 tool, equipped with a z-stage for vertical stage control for a proper field correction. A series of different base doses were done to find the correct dose. The beam energy was 50 keV, and the probe current was 6 nA using a 300 μm aperture. The Si sample was spin-coated with a 150 nm thick resist layer of 495 PMMA in 3% Anisole. It was soft-baked for 10 min at 180 °C. After the exposure, at 0° and 17° tilt, it was developed for 60 s in MIBK, rinsed for 60 s with IPA and dried with dry nitrogen gas. After development inspection was done in a Thermo Fisher Scientific Helios G4 CX DualBeam™ SEM. The detector used was the through the lens detector in secondary electron mode with beam deceleration (−50 V stage bias).

Figure 17 shows an SEM image of the exposed areas after development. The dark (black) tones represent PMMA resist and the bright (white) ones the silicon substrate. The upper block was exposed by taking the tilt correction into account; the lower block was not corrected for tilt but had the standard PEC applied.

It is observed that the lines (five on each side) were exposed and developed properly at both the left- and the

right-hand sides of the squares. In Figs. 18 and 19, the lhs structures and the rhs structures are magnified to allow measurement of the linewidths, or critical dimension (CD). Note that the bright structures are in fact trenches, but we call them lines for convenience.

To measure the linewidths from these images, the intensity profiles across the top and bottom lines, integrated over 100 pixels, are plotted in Fig. 20. The signals do not look like the typical top-down inspection image signals of Manhattan structures.[26] They reveal multiple features such as peaks, dips, and glitches. These features arise from the fact that the tilted exposure also results in lines with tilted sidewalls after development, as schematically shown in Fig. 21. Here, the cross-sectional and top-down views are shown for line shapes resulting from tilted and nontilted exposures. The tilted exposure leads to the rhombuslike cross section of the lines, originating from the left-shift of the short-range peak visible in Figs. 9 and 10. Therefore, measuring the linewidths of these rhombuslike lines is less straight-forward than measuring the widths of the lines exposed without tilt, for which the standard CD measurement protocols[27] can be used.

We adopted a simple CD measurement protocol, based on the cartoon of Fig. 22, where the exposed regions are shown as trenches. The left and right peaks in the SEM linescan signal (the red circles in Fig. 22 in the color online version) are identified as the edge positions on the top surface of the resist (the green dots on resist corners in Fig. 22 in the color
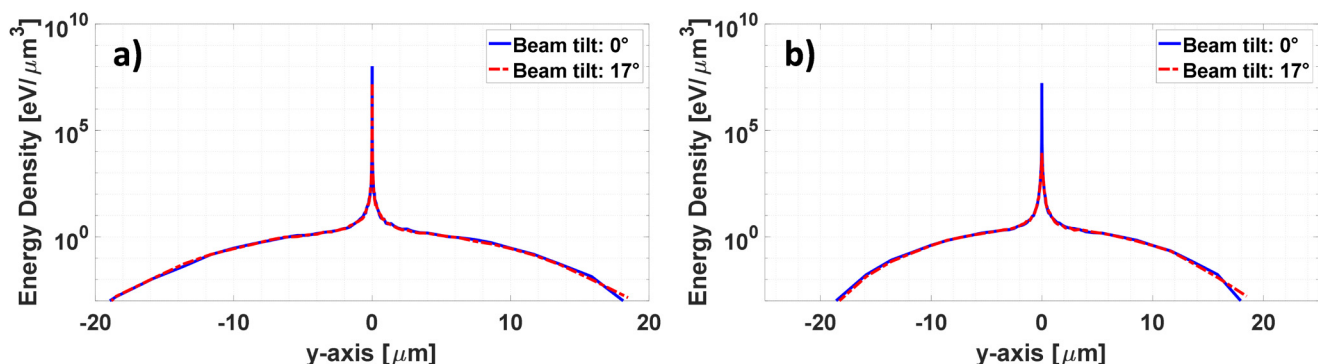

FIG. 12. Comparison of the PSFs on a linear scale along the y-axis, to show the symmetry: (a) in the top-most layer (vacuum interface) and (b) in the bottom layer (substrate interface).
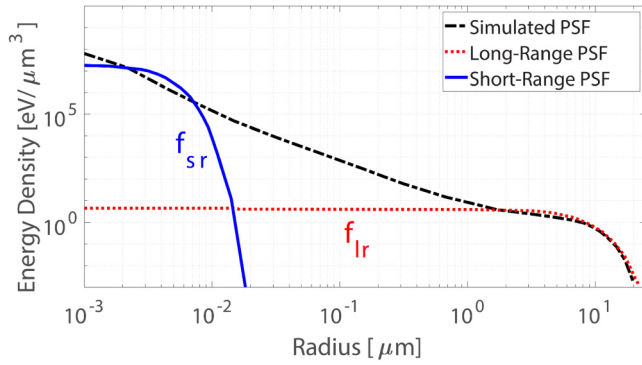
FIG. 13. Comparison of simulated PSF, which was calculated by Monte Carlo simulator and approximated PSF is used in PEC.
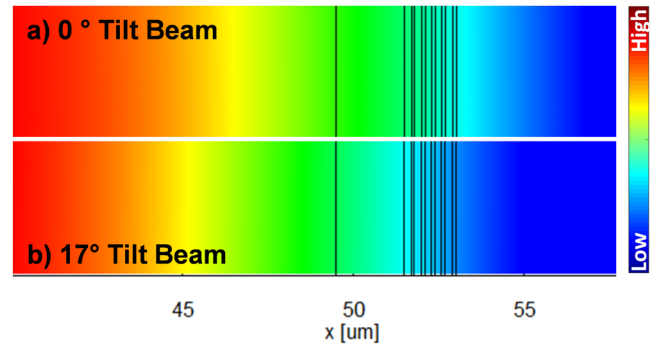

FIG. 14. Long-range dose distribution: (a) nontilted beam and (b) 17° tilted beam. The color map represents the amount of dose received by the resist. To obtain the distribution for the 17° tilted beam exposure, the distribution for the nontilted beam exposure is shifted left by 2.1 μm. The dense narrow lines on the right are part of the geometry shown in Fig. 7, and the leftmost isolated line indicates the boundary between areas of constant dose.

online version). The CD is then taken as the distance between these peaks. The red circles are also indicated in Fig. 20, from which the CDs are determined. The values are collected in Fig. 23 together with the CDs of the lines resulting from the nontilted exposures.

Figure 23(a) shows the linewidths (of the trenches) for exposure without tilt correction and Fig. 23(b) shows the linewidths for exposure with tilt correction. The lines 1 to 5 are ordered from left to right. Notice that, the first line on the lhs and the fifth line on the rhs are the outermost structures.

In Fig. 23(a), it is seen that the lines left of the big square are wider than those to the right of the square. Since the deposited doses are the same [see the dose map in Fig. 16(c)], the observed difference indicates the asymmetry in the dose distribution. The following explanations can be made on this structure to describe the phenomenon in details:

• The lhs lines received a larger long-range dose contribution than the rhs lines, considering that the long-range PSF is left-shifted by 2.1 μm.
• On the rhs, the linewidth of the third line is larger than that of the fourth and fifth lines, even though the short-range dose contribution is lower [see Fig. 16(c)]. This could be explained by the larger long-range dose

contribution to the third line exposure when exposing the fourth and fifth lines, the total (short + long range) contribution reaching a maximum at the third line.
• The linewidth of the first and the second lines is smaller than the others on the rhs. This is because both short-range and long-range contributions decrease when the e-beam moves to the left.
• On the lhs, the first line is the widest. This is mainly due to the strong short-range dose contribution. Secondly, the long-range contribution to the first line when exposing the lines to the right of the first line (still at the lhs) increases, the dose increasing gradually going left toward to first line.
• On the lhs, the fourth and the fifth lines are slightly wider than the third line. Although the short-range dose contribution decreases going right [Fig. 16(c)] the long-range dose contribution when exposing the high-density square pattern to the right of the fifth line contributes strongly to the exposure of the fourth and fifth lines. For the third line, the short-range dose contribution is larger than for the fourth and the fifth lines, but the long-range dose contribution, when exposing the patterns to the right of the
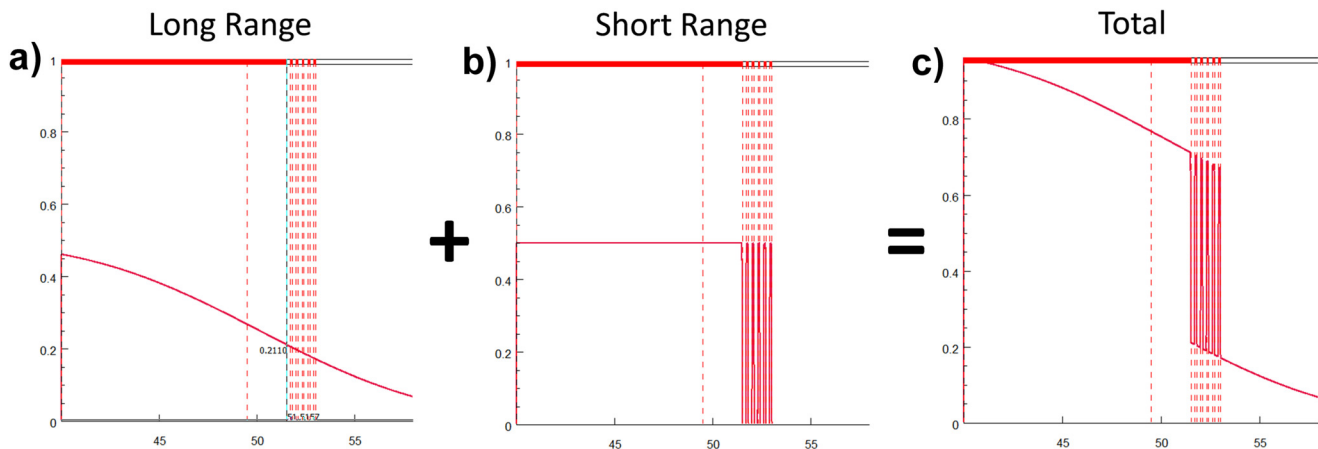

FIG. 15. Total dose distribution. The dashed narrow vertical lines denote the lines of the test pattern. (a) The normalized long-range dose distribution; (b) the normalized short-range dose distribution; and (c) the total dose distribution for the 17° tilted beam exposure.
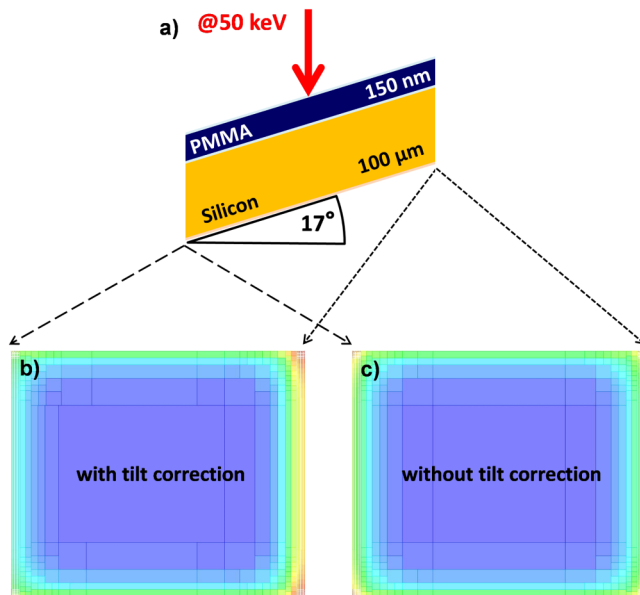
FIG. 16. PEC (a) shows the experimental setup, (b) the dose map calculated when tilt is considered in PEC, and (c) the dose map calculated using the standard PEC. The color maps show the variation of dose over the pattern. Red (corners) and blue (in color online version) correspond to 1.58 and 0.70 relative base dose.

FIG. 18. Lines at the left-hand side imaged at a higher magnification. The lines of the upper block were exposed with tilt correction. The lines of the lower block were exposed without tilt correction.

third line, decreases more than the short-range dose contribution can compensate for.

When comparing Figs. 23(a) and 23(b):

- The rhs lines are wider when correcting for the tilt, as expected, because the base dose is increased to compensate for the asymmetric PSF.
- For the same reason, the lhs lines received less dose in the tilt corrected case, and therefore they are narrower than in the noncorrected case.

Looking at Fig. 23(b), the widths of the rhs lines are slightly larger (~11 nm) than the lhs lines, although they are expected to be the same when taking the tilt correctly into

account in the PEC. We think that this might be due to an overcorrection caused by the approximate PSF. In Fig. 13, it is seen that in the mid-range between 10 nm and 1 μm the approximate PSF used in the PEC is lower than the simulated PSF. This may enhance the short-range, and indirectly, the long-range dose effects during the PEC. It causes a directional effect in the tilt ($-$x) direction, in each block (rhs or lhs), a line located at the left always receives a larger total dose than any other lines in that block.

VI. DISCUSSION

We have shown that the PSF for exposure of a tilted surface is different than for perpendicular exposure. From the proof of principle experiments presented here, it is clear that standard PEC algorithms have to be adapted for the different PSF when exposing curved or tilted surfaces. It will improve the accuracy in the fabrication of nanostructures on such surfaces. Its effect will even be more prominent when
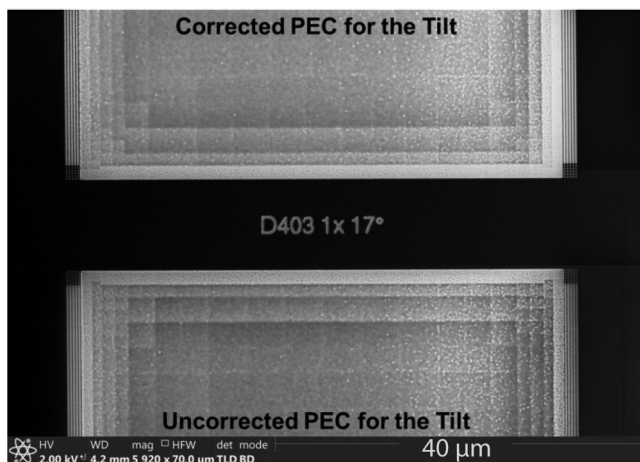

FIG. 17. Two identical patterns were written on PMMA resist. A PEC algorithm which uses a PSF corrected for the tilt was applied for the top block, and a PEC algorithm with a standard PSF is applied for the bottom block.
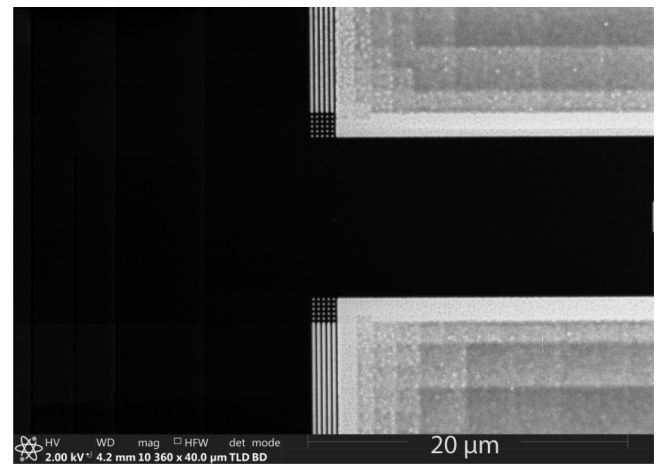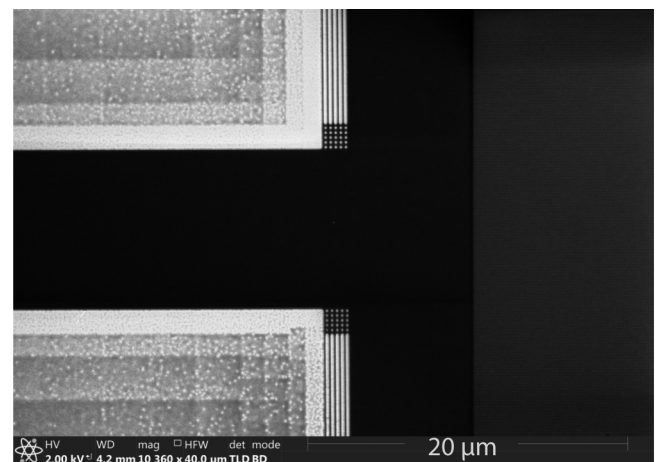

FIG. 19. Lines at the right-hand side imaged at a higher magnification. The lines of the upper block were exposed with tilt correction. The lines of the lower block were exposed without tilt correction.
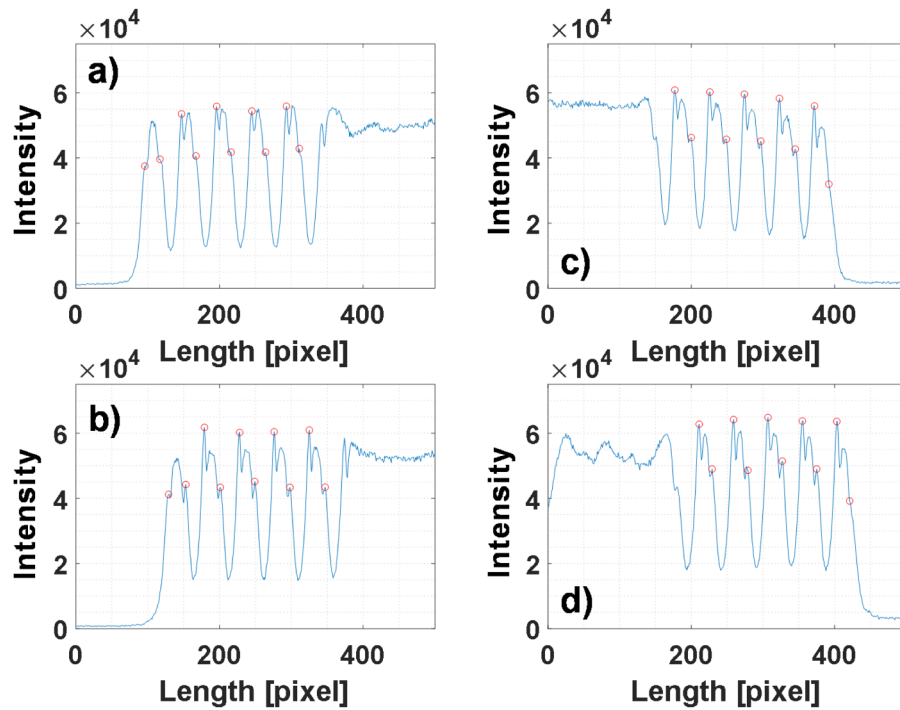
FIG. 20. Integrated linescan profiles: (a) upper lines of Fig. 18, (b) lower lines of Fig. 18, (c) upper lines of Fig. 19, and (d) lower lines of Fig. 19. The pixel size is equal to 6.5 nm. The red circles indicate the edges depicted by solid dots (green in the online color version) in Fig. 22.

using resist layers thicker than 150 nm, a beam energy lower than 50 keV, or an angle of incidence larger than 17°.

In this study, an energy deposition model was used to determine the number of broken bonds in the resist. However, it would be more realistic to consider individual bond breaking events.[28] Knowledge of the bond-breaking cross sections, or how to separate them from inelastic scattering cross sections, would help in achieving a more reliable PSF. However, such knowledge is still limited[23,28,29] even for well-known polymers such as PMMA.

In addition, in the PEC applied in this work, we have neglected the short-range effect, arguing that we expect this to be a minor effect for structure sizes of 100 nm or more. However, it should be considered for the fabrication of much smaller structures.

In the experiments, the big square structure in the middle is not fully bright in the SEM images and the inner borders (smaller squares) are visible. These regions were underexposed for the dose applied ($403 \, \mu C/cm^2$), but the smaller structures (lines) on the sides are overexposed at this dose. We assume that there is an imbalance between the short- and long-range dose distributions used in the tilt-corrected version, where the magnitude of the short-range dose is underestimated and the magnitude of the long-range effect is overestimated. However, the CD values of the lines on each side of the square are most relevant for this study and they
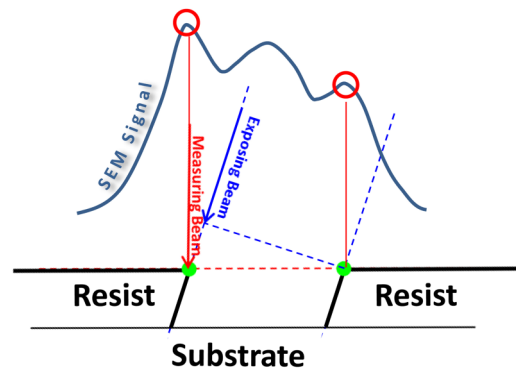
FIG. 22. CD measurement protocol for the tilted lines. Exposure was done on a tilted sample along the tilted (blue) dashed line producing a trench with a nominal width of 100 nm (between the green solid dots). The inspection was done without a tilt such that the electron probe scans along the (red) horizontal dashed line. The nominal value of the measured width is 105 nm due to the uncorrected projection. The resulting SEM line scan signal is depicted above the geometry. The peaks (red empty circles) in the SEM signal correspond to the edges indicated by the (green) filled dots. Colors are visible on the online version.
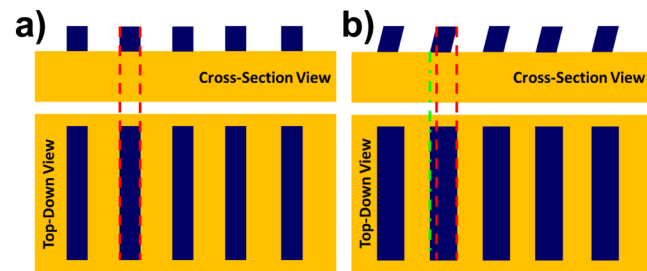

FIG. 21. Shape of the resist lines. The yellow region represents the substrate; dark blue regions are the resist lines. (a) The images show the cross-sectional and top-down views of lines exposed without tilt. (b) The images show the cross-sectional and top-down views of the lines exposed with tilt. The dashed red lines are guides to the eye to judge the linewidth from the cross-sectional view. The dotted green line on the right shows the linewidth as judged from the top-down view.
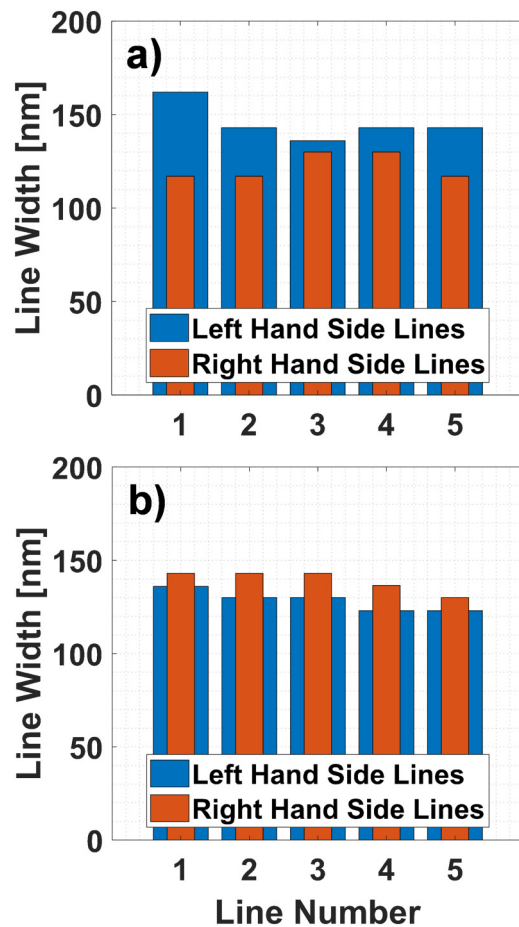
FIG. 23. Comparison of CDs: (a) PEC without tilt correction, (b) PEC with tilt correction.

are resolved well enough at this dose to perform a quantitative analysis. The CD comparison for the uncorrected exposure [Fig. 23(a)] demonstrates the asymmetry in the PSF. The rhs lines receive less dose than the lhs lines. The adjustment made to the PEC kernel overestimates the tilt effect and leads to wider lines on the right side than on the left side [Fig. 23(b)]. However, the difference in CD between the right and left sides is less in the corrected version compared to the uncorrected version.

Lastly, the asymmetric 3D PSF has been simplified into 2D, for the direction of the incident beam (−x), for ease of implementation, but a convolution kernel which uses the full 3D PSF will improve the accuracy and will solve the issues indicated above, especially for 3D structures such as circles or squares.

VII. CONCLUSION

There is a growing interest in patterning nanostructures on curved or tilted surfaces using EBL. However, standardly used PSFs and PEC algorithms, developed for perpendicular patterning on flat surfaces, are not suitable for such applications.

In this study, we have demonstrated that the PSF is not radially symmetric for the exposure of tilted surfaces, using Monte Carlo simulations. The asymmetry is confirmed by a proof of principle experiment for a single point exposure.

To verify the effect more quantitatively, the nonsymmetric PSF was calculated, using simulations, and a PEC algorithm was adjusted for the exposure of a tilted substrate. A test pattern was written with and without PEC correction for tilted surfaces. The results show that it is possible to improve the fabrication accuracy in terms of critical dimension by taking the asymmetric PSF into account.

[1]J. M. Pavkovich, J. Vac. Sci. Technol. B **4**, 159 (1986).
[2]M. Parikh, J. Appl. Phys. **50**, 4378 (1979).
[3]G. Owen, J. Vac. Sci. Technol. B **8**, 1889 (1990).
[4]J. Zhou and X. Yang, J. Vac. Sci. Technol. B **24**, 1202 (2006).
[5]M. Stepanova, T. Fito, Z. Szabó, K. Alti, A. P. Adeyenuwo, K. Koshelev, M. Aktary, and S. K. Dew, J. Vac. Sci. Technol., B **28**, C6C48 (2010).
[6]Q. Dai, S. Y. Lee, S. H. Lee, B. G. Kim, and H. K. Cho, Microelectron. Eng. **88**, 3054 (2011).
[7]Q. Dai, S.-Y. Lee, S.-H. Lee, B.-G. Kim, and H.-K. Cho, J. Vac. Sci. Technol. B **29**, 06F314 (2011).
[8]V. R. Manfrinato *et al.*, Nano Lett. **14**, 4406 (2014).
[9]T. H. P. Chang, J. Vac. Sci. Technol. **12**, 1271 (1975).
[10]S. A. Rishton and D. P. Kern, J. Vac. Sci. Technol. B **5**, 135 (1987).
[11]D. Wilson, P. Maker, R. Muller, P. Mourolis, M. Descour, C. Volin, and E. Dereniak, *Diffractive Optics and Micro-Optics*, edited by T. Li (OSA Trends in Optics and Photonics, Québec City, 2000).
[12]D. W. Wilson, P. D. Maker, R. E. Muller, P. Mouroulis, and J. Backlund, Proc. SPIE **5173**, 115 (2003).
[13]W. R. Johnson, S. J. Hook, S. S. Shoen, and B. T. Eng, "Hyperspectral Thermal Emission Spectrometer: Engineering Flight Campaign," In IEEE Aerospace Conference (2013), Vol. 91109, pp. 1–7.
[14]B. Van Gorp, P. Mouroulis, D. W. Wilson, and R. O. Green, Proc. SPIE **9222**, 92220C (2014).
[15]P. Mouroulis *et al.*, Appl. Opt. **53**, 1363 (2014).
[16]S. J. Wind, P. D. Gerber, and H. Rothuizen, J. Vac. Sci. Technol. B **16**, 3262 (1998).
[17]T. Verduin, "Quantum noise effects in e-beam lithography and metrology," Doctoral thesis (Delft University of Technology, 2016).
[18]M. A. Mohammad, M. Muhammad, S. K. Dew, and M. Stepanova, *Nanofabrication: Techniques and Principles* (Springer, Vienna, 2011), pp. 11–41.
[19]F. Salvat, A. Jablonski, and C. J. Powell, Comput. Phys. Commun. **165**, 157 (2005).
[20]E. Schreiber and H. J. Fitting, J. Electron Spectrosc. Relat. Phenom. **124**, 25 (2002).
[21]E. Kieft and E. Bosch, J. Phys. D: Appl. Phys. **41**, 215310 (2008).
[22]J. P. Ganachaud and A. Mokrani, Surf. Sci. **334**, 329 (1995).
[23]B. Wu and A. R. Neureuther, J. Vac. Sci. Technol. B **19**, 2508 (2001).
[24]N. Unal, D. Mahalu, O. Raslin, D. Ritter, C. Sambale, and U. Hofmann, Microelectron. Eng. **87**, 940 (2010).
[25]GenISys GmbH, https://www.genisys-gmbh.com.
[26]J. Bolten, K. T. Arat, N. Ünal, C. Porschatis, T. Wahlbrink, and M. C. Lemme, Proc. SPIE **10446**, 83–88 (2017).
[27]Y. G. Li, P. Zhang, and Z. J. Ding, Scanning **35**, 127 (2013).
[28]M. Aktary, M. Stepanova, and S. K. Dew, J. Vac. Sci. Technol. B **24**, 768 (2006).
[29]P. Kruit and S. Steenbrink, J. Vac. Sci. Technol. B **23**, 3033 (2005).